

Cite this: *Energy Environ. Sci.*,  
2026, 19, 870

# Helical counter-directional migration-induced solvation sheaths for constructing reinforced electrode–electrolyte interphases for ultra-stable anode-free lithium metal batteries

Yunyi Chen,<sup>abc</sup> Xitang Qian,<sup>ab</sup> Yuxiang Lyu,<sup>ab</sup> Yican Qiu,<sup>ab</sup> Yee Tung Kwan,<sup>a</sup>  
Siyu Zhou,<sup>ab</sup> Xinyi Lan,<sup>ab</sup> Siqi Lu<sup>ab</sup> and Minhua Shao<sup>ab\*</sup>

Anode-free lithium metal batteries hold great potential for high-capacity energy storage by eliminating both the conventional graphite anode and any excess lithium metal. However, irreversible charge–discharge cycles lead to the rapid depletion of active lithium inventories. Moreover, ether-based electrolytes suitable for the anode-free configuration are unstable at high voltages, which makes them incompatible with high-nickel cathodes and ultimately curtails their role in enhancing energy density. This study proposes an interface modification strategy driven by helical counter migration. During the formation process, ion movement pathways and anion–cation association effects regulated by internal forces generated by a magnetized nickel-coated current collector synergistically guide anions into solvation structures of the adjacent lithium ions migrating in the opposite direction, thereby forming a mechanically robust ion-permeable solid electrolyte interphase, which is characterized by an ordered inorganic particle skeleton infused with organic components, similar to the structure of reinforced concrete. Consequently, the helical counter-directional migration-assisted copper electrode achieves a coulombic efficiency of 99.9%. The assembled anode-free Cu||LiFePO<sub>4</sub> cell maintains over 80% capacity retention after 200 cycles, and the anode-less Cu||LiFePO<sub>4</sub> cell sustains stable operation for over 1000 cycles. Furthermore, the internal electric field drives helical counter-directional migration-induced anion-derived solvation sheaths to diffuse to the cathode side and optimize the cathode–electrolyte interphase, enabling stable operation of high-nickel cathodes. Anode-free Cu||NCM811 cells cycled at 4.5 V exhibit a capacity retention exceeding 75% after 100 cycles and realize a 453.5 Wh kg<sup>-1</sup> anode-free lithium metal pouch cell configuration.

Received 18th October 2025,  
Accepted 18th December 2025

DOI: 10.1039/d5ee06208j

rsc.li/ees

## Broader context

The global transition towards sustainable energy and electrified transportation is dependent on the development of next-generation energy storage systems with higher energy densities than current lithium-ion technology. Anode-free lithium metal batteries, which eliminate the conventional graphite anode and excess lithium, offer a promising solution for high-capacity storage. However, their cycle life is limited by rapid depletion of active lithium due to irreversible side reactions. A crucial approach is to develop a robust solid electrolyte interphase (SEI) to enable uniform lithium deposition and stripping, though this poses significant challenges. Additionally, ether-based electrolytes, though suitable for anode-free designs, tend to decompose at high voltages. It is also necessary to create a stable cathode–electrolyte interphase (CEI) that can reduce side reactions and expand the electrochemical window. This study presents an effective strategy using surface modification through the HCMASS. This method guides electrolyte ion migration during formation, enriching anions in the solvation sheaths of lithium ions. This process results in a robust SEI with an ordered inorganic skeleton infused by organic components, exhibiting exceptional mechanical strength and high ionic permeability. Notably, the HCMASS also optimizes the CEI layer, enabling stable operation of NCM811 cathodes in ether-based electrolytes. This coordinated regulation of both interfaces allows a 2.45 Ah anode-free Cu||NCM811 battery to achieve an energy density over 453.5 Wh kg<sup>-1</sup>.

<sup>a</sup> Department of Chemical and Biological Engineering, The Hong Kong University of Science and Technology, Clear Water Bay, Kowloon, Hong Kong 999077, China.  
E-mail: kemshao@ust.hk

<sup>b</sup> Energy Institute, The Hong Kong University of Science and Technology, Clear Water Bay, Kowloon, Hong Kong 999077, China

<sup>c</sup> Guangzhou Key Laboratory of Electrochemical Energy Storage Technologies, Guangzhou HKUST Fok Ying Tung Research Institute, Guangzhou 511458, China

<sup>d</sup> CIAC-HKUST Joint Laboratory for Hydrogen Energy, The Hong Kong University of Science and Technology, Clear Water Bay, Kowloon, Hong Kong 999077, China

# 1. Introduction

Lithium metal anodes, boasting a theoretical specific capacity ( $3860 \text{ mAh g}^{-1}$ ) ten-fold higher than graphite anodes, are recognized as a key anode candidate for achieving theoretical energy densities exceeding  $500 \text{ Wh kg}^{-1}$ .<sup>1,2</sup> Adopting an anode-free configuration can maximize the advantages of lithium metal batteries. However, the formation of dendrites and isolated lithium caused by non-uniform lithium-ion aggregation is prone to continuous loss of active lithium and severe safety concerns,<sup>3,4</sup> thus posing a key technical obstacle to the development of high energy density anode-free lithium metal batteries (AFLMBs).<sup>5-7</sup>

Research has shown that optimizing the electrode–electrolyte interphases can effectively regulate lithium-ion distribution and mitigate active lithium depletion.<sup>8-10</sup> Strategies include employing functional additives to increase the solid–electrolyte interphase (SEI) composition for improved lithium-ion diffusion kinetics<sup>11-13</sup> or constructing artificial protective layers (*via in situ/ex situ* methods) to reinforce interfacial mechanical strength against vertical dendrite propagation.<sup>14-16</sup> Despite these advancements, complete suppression of the heterogeneous nucleation and growth of lithium remains elusive. Fundamental improvements require addressing the root mechanisms of the formation of non-uniform deposition structures such as dendrites and rods.

Our previous studies reveal that the non-uniform lithium ion flux caused by the anisotropy of the SEI is the main driving factor for dendrite/rod formation.<sup>17</sup> Although we have previously utilized external physical fields to achieve uniform interfacial lithium distribution,<sup>18-20</sup> the SEI remains susceptible to volume changes during charge/discharge cycles under anode-less conditions, trapped in a detrimental cycle of “fracture–reformation–fracture”. Additionally, ether-based electrolytes, which are generally suitable for anode-free configurations, are prone to decomposition when operated at high voltage. It is also necessary to find a suitable strategy to simultaneously construct a cathode–electrolyte interphase (CEI) that can suppress persistent side reactions to help broaden the electrochemical window.

In this work, we present tailored helical counter-directional migration-induced anion-derived solvation sheaths (HCMASS) for the concurrent optimization of the SEI and CEI structure and composition (Fig. 1). The non-uniform electrode surface induces curvature in the electric field distribution, attracting deflection in the migration trajectories of electrolyte cations/anions. A magnetized nickel layer coated on copper foil causes the ions to move at an angle relative to the magnetic field vector, resulting in a helical motion driven by an external force. Interestingly, anions tend to infiltrate the solvation structures of adjacent lithium ions while displacing neutral solvent

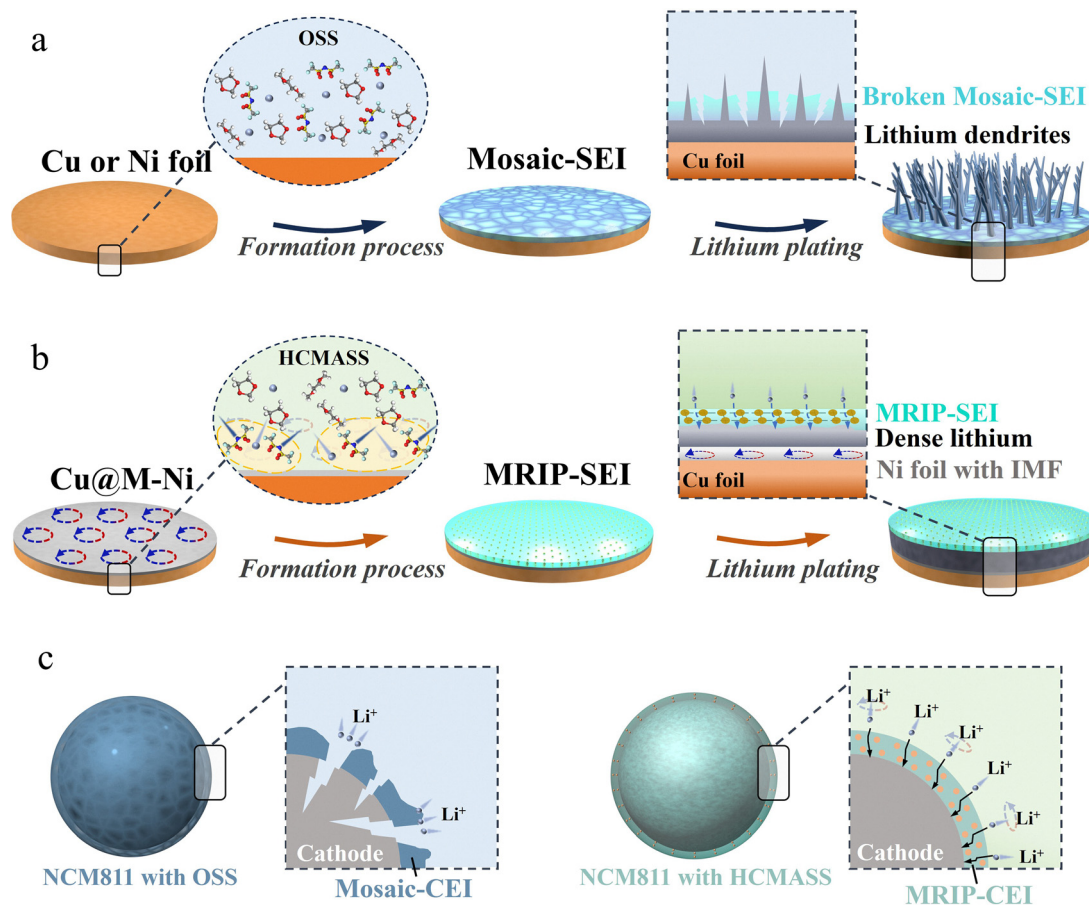


**Fig. 1** Magnetized nickel-layer-induced HCMASS facilitating uniform lithium deposition. Schematic of lithium plating behavior on (a) Cu or Ni foil and (b) M–Ni coating. (c) Insertion and extraction behaviors of lithium ions in NCM811 with or without M–Ni coating.

molecules, thereby forming the HCMASS. These aggregated HCMASS preferentially form inorganic cluster nuclei at the current collector surface, subsequently interconnected by solvent reduction-derived organic components to create a reinforced steel-concrete-like mechanically robust ion-permeable SEI (MRIP-SEI) (Fig. 1b). *In situ* Raman spectroscopy verifies that the magnetized nickel (M-Ni) coating regulates interfacial solvation structures and strong anion adsorption characteristics. Characterization techniques, including depth-profiling X-ray photoelectron spectroscopy (XPS), time-of-flight secondary ion mass spectrometry (ToF-SIMS), and cryogenic transmission electron microscopy (cryo-TEM), validate the unique composition and architecture of this engineered SEI. Compared with the conventional mosaic-type SEI, this hybrid structure demonstrates superior ionic conductivity and mechanical resilience, attributed to inorganic fillers providing structural support, while organic binders enable elastic deformation. The organic-inorganic phase boundaries facilitate rapid lithium-ion transport, as evidenced by comprehensive electrochemical analysis. The HCMASS-assisted current collector achieves an exceptional coulombic efficiency (CE) of 99.9% at 1 mA cm<sup>-2</sup>. When implemented in anode-less full cells (negative/positive capacity ratio = 0.8), stable cycling over 1000 cycles is maintained with >80% capacity retention. Notably, the internal electric field (IEF) during the discharge process drives the HCMASS to diffuse to the cathode side and optimize the cathode-electrolyte interphase, forming a protective layer that combines robust mechanical properties with high lithium-ion conductivity, inhibiting the transition-metal dissolution (Fig. 1c). The innovation allows stable operation of LiNi<sub>0.8</sub>Co<sub>0.1</sub>Mn<sub>0.1</sub>O<sub>2</sub> (NCM811) cathode materials while maintaining structural integrity. This advancement enables the anode-free Cu||NCM811 pouch cell (~2.45 Ah) configuration to deliver an energy density of 453.5 Wh kg<sup>-1</sup>. This work provides fundamental insights into HCMASS-assisted SEI engineering and demonstrates a practical pathway toward high-energy-density AFLMBs.

## 2. Results and discussion

### 2.1 Regulation of the solvation structure by the magnetized nickel layer to form HCMASS

In conventional ether-based electrolyte systems, lithium ions interact with anions and solvent components, resulting in the formation of an ordinary solvation sheath structure (OSS) composed of solvent-anion complexes (Fig. 2a).<sup>21</sup> This solvation sheath diffuses alongside Li<sup>+</sup> and preferentially undergoes reduction upon contact with the anode surface, leading to the formation of a mosaic-structured SEI.<sup>22,23</sup> This study introduces an internal Lorentz force (ILF) through magnetized nickel-coated foils. The inherent surface heterogeneity of electrodes induces an electric field curvature, creating an angular relationship between the motion trajectories of charged Li<sup>+</sup>/TFSI<sup>-</sup> species and the magnetic field direction.<sup>24</sup> ILF-driven counter-rotational dynamics facilitate anion penetration into adjacent Li<sup>+</sup> solvation sheaths, ultimately forming HCMASS, as shown in Fig. 2a.

COMSOL simulations were employed to confirm the helical motion of ions near the anode surfaces. As shown in Fig. 2b, the paths of charged particles deflect under the influence of the ILF, resulting in the reconstruction of the original solvation structure. In contrast, such behavior is not observed in the control case (Fig. 2c). Furthermore, to validate that this helical motion promotes the entry of anions into the solvation sheath of Li<sup>+</sup> ions moving in the opposite direction, molecular dynamics (MD) simulations and *in situ* Raman spectroscopy were used to investigate the ether-based electrolyte chemistry under different conditions. The radial distribution functions (RDF) and coordination numbers (CNs) of Li<sup>+</sup>-O (TFSI<sup>-</sup>) are derived from MD simulations to explore the coordination of Li<sup>+</sup> with and without ILF (Fig. S1, SI). After applying an ILF in the simulation system, both the height and area of the first peak in the RDF increase, suggesting a rise in the CNs of TFSI<sup>-</sup> around the Li<sup>+</sup>. By integrating the  $g(r) - r$  plot, the variation of CNs with  $r$  is obtained, as shown in Fig. S1a-c, SI. Further calculations reveal that under the influence of ILF, the Li<sup>+</sup>-O (TFSI<sup>-</sup>) coordination number increases from 1.73 to 2.12 (Fig. S1d, SI). This indicates that spiral migration leads to more anions entering the solvation sheaths of adjacent lithium ions moving in the opposite direction. Raman spectroscopy was also used to explore the solvation sheaths. Quantitative analysis reveals distinct TFSI<sup>-</sup> participation ratios in solvation structures: 26.7% for Cu foil, 46.2% for Ni-coated electrodes, and enhanced 79.6% under the M-Ni configuration (Fig. 2d, e and Fig. S2, SI), demonstrating strengthened cation-anion association. This conclusion is consistent with the results obtained from Fourier transform infrared (FTIR) spectroscopy (Fig. S3, SI). A systematic investigation was conducted to examine the effects of the nickel layer thickness and magnetic flux density on lithium-ion/anion coordination. Through electrodeposition of nickel layers (0.1–3 μm thickness range) on Cu foil followed by 180 days of magnetization achieving 5–15 mT flux density (Fig. S4 and S5, SI), Raman spectroscopy reveals an optimal TFSI<sup>-</sup> coordination trend. The coordination between Li<sup>+</sup> and anions progressively enhances as the nickel thickness increases from 0.1 μm (5 mT) to 1 μm (10 mT). However, further thickness increases (1–3 μm, 10–15 mT) result in coordination decline due to electrostatic interactions (Fig. 2f and Fig. S6, SI). Comprehensive electrochemical testing and morphological characterization on current collectors with varying nickel thicknesses after formation demonstrate that Li||Cu@Li cells with 1 μm-thick nickel layers achieve the most favorable performance metrics: lowest interfacial impedance (45.7 Ω), highest CE (99.9%), and densest lithium deposition morphology (Fig. S7–S9, SI). Therefore, a nickel layer thickness of 1 μm is selected as the optimal choice for subsequent studies. These findings indicate that the optimized HCMASS creates an advantageous interfacial microenvironment for lithium plating/stripping processes.

HCMASS also demonstrates an enhanced capability to induce anion decomposition at the interface, as confirmed by linear sweep voltammetry (LSV) measurements. The TFSI<sup>-</sup> decomposition current on the M-Ni surface reaches 0.48 mA, higher than those observed on the Cu foil (0.10 mA) and non-magnetized



**Fig. 2** Li<sup>+</sup> solvation structure under the action of the M–Ni layer. (a) Schematic diagram of the solvation structures on copper and non-magnetized nickel foil surfaces (yellow), as well as those on magnetized nickel foil surfaces (blue). Simulation results for the different trajectories of Li<sup>+</sup> during the ion diffusion process (b) with M–Ni and (c) Ni or Cu. Raman spectra of TFSI<sup>-</sup> with (d) Ni and (e) M–Ni. (f) The proportion of free TFSI<sup>-</sup> in the solvated sheath under different magnetized nickel layer thickness conditions. (g) LSV curves of Li||Cu cells with various current collectors. (h) Schematic diagram of an *in situ* Raman test cell. (i) *In situ* Raman spectra of Li<sup>+</sup>–TFSI<sup>-</sup> during cycles with M–Ni. (j) *In situ* Raman curves during charging/discharging cycles with M–Ni.

Ni layer (0.19 mA) (Fig. 2g). Furthermore, the reduction potential of TFSI<sup>-</sup> on M–Ni exhibits an anodic shift, indicating more favorable decomposition kinetics under these conditions. To validate the stability of HCMASS induced by the M–Ni coating, we designed an electrochemical cell for *in situ* Raman spectroscopy monitoring during galvanostatic cycling (Fig. 2h). The persistent Li<sup>+</sup>–TFSI<sup>-</sup> interaction is evidenced by the stable Li<sup>+</sup>–TFSI<sup>-</sup> Raman shifts at 745 cm<sup>-1</sup> throughout cycling, suggesting the dominance of contact ion pairs (CIPs) in the solvation structure (Fig. 2i). Both solvent molecules and anions maintain stable Raman signatures during charge/discharge processes, confirming the exceptional stability of HCMASS (Fig. 2j). In contrast, the OSS exhibits inferior

stability with dynamic Free-DOL characteristics (~730 cm<sup>-1</sup>), showing cycle-dependent “appearance–disappearance–decay” behavior (Fig. S10, SI). This indicates that interfacial instability may lead to the anisotropic composition, structure, and properties in OSS-derived SEI layers.<sup>25</sup>

## 2.2 Optimizing the SEI layer composition and structure through HCMASS

The HCMASS can help facilitate interfacial generation of abundant inorganic constituents through anion-dominated solvation sheaths. These inorganic components aggregate into uniformly distributed nanoparticles under interfacial micro-magnetic field

effects, as jointly validated by cryo-TEM (Fig. S11, SI), XPS depth profiling, and ToF-SIMS. Firstly, cryo-TEM shows that the HCMASS-induced MRIP-SEI demonstrates superior uniformity with an  $\sim 25$  nm thickness, satisfying electron tunneling suppression criteria<sup>26</sup> (Fig. 3a), while the OSS-derived SEI exhibits an irregular undulating morphology with thickness fluctuations (Fig. 3b), detrimental to homogeneous  $\text{Li}^+$  transport. High-resolution cryo-TEM imaging reveals that inorganic substances in the MRIP-SEI are assembled into  $\sim 2$ – $4$  nm particles with

ordered alignment, forming a robust “reinforced concrete-like” SEI architecture (Fig. 3c). In contrast, the OSS-SEI displays amorphous characteristics corresponding to organic-rich interfacial layers (Fig. S12a, SI). Through calibration of surface-proximal lattices in cryo-TEM images and measurement of lattice spacings in inverse fast Fourier transform (FFT) patterns (Fig. 3d and Fig. S13, SI), abundant inorganic components are identified in the MRIP-SEI including  $\text{LiF}(111)$ ,  $\text{LiF}(200)$ ,  $\text{Li}_2\text{S}(200)$ , and  $\text{Li}_2\text{O}(111)$  (Table S1, SI). These findings corroborate our proposed



**Fig. 3** Composition distribution of the MRIP-SEI layer induced by the HCMASS. Cryo-TEM images of (a) MRIP-SEI (M–Ni) and (b) Ni-SEI morphologies (scale bar: 20 nm). (c) High-resolution cryo-TEM images of the MRIP-SEI (scale bar: 5 nm). (d) Inverse FFT images of the MRIP-SEI (scale bar: 1 nm). (e) SAED pattern of the regions at the surface of growth lithium (scale bar:  $5 \text{ nm}^{-1}$ ). (f) High-resolution XPS depth profiles of the formed MRIP-SEI (M–Ni) of F 1s. (g) The atomic composition ratios of the MRIP-SEI varying with the sputtering time. (h) XPS spectra of O 1s of the MRIP-SEI and Ni-SEI. (i) TOF-SIMS 3D distribution of the MRIP-SEI (M–Ni). Depth profiles of (j) the MRIP-SEI and (k) the Ni-SEI. Single-color gradient maps of  $\text{LiF}_2^-$ ,  $\text{LiCO}_3^-$ ,  $\text{LiS}^-$ , and  $\text{LiO}^-$  in (l) the MRIP-SEI and (m) the Ni-SEI.

MRIP-SEI formation mechanism: anion-aggregated solvation sheaths preferentially react to generate inorganic species that coalesce into nanoparticles under magnetic field guidance, subsequently interconnected by organic byproducts from solvent reduction, ultimately forming a LiF-rich inorganic–organic interfacial passivation layer with an ordered structure. Selected area electron diffraction (SAED) patterns confirm polycrystalline features, with concentric rings corresponding to LiF, Li<sub>2</sub>O, Li<sub>3</sub>N, and Li<sub>2</sub>S phases (Fig. 3e). To assess the structural stability of the SEI, we systematically characterized lithium morphologies post-cycling on different substrates. The interfacial passivation layers on conventional Cu foils show indistinguishable structural features (Fig. S12b, SI), likely due to uneven lithium deposition/stripping behaviors that severely compromise the fragile OSS-SEI layers. Conversely, the MRIP-SEI maintains its dense outer structure with a preserved original morphology even after multiple lithium-ion transits (Fig. S12c, SI). Lattice calibration and FFT pattern analysis of the MRIP-SEI after cycling (Fig. S14, SI) confirm persistent retention of inorganic components after prolonged cycling.

The XPS spectra of F 1s consistently exhibit a prominent peak at 685 eV binding energy throughout the SEI layer (Fig. 3f), indicating a high inorganic content of LiF.<sup>27</sup> Time-resolved sputtering analysis reveals that fluorine maintains dominant proportions (45–50%) across the SEI thickness, exceeding other elemental ratios, confirming LiF-rich SEI formation (Fig. 3g). The LiF fraction in F 1s spectra reaches 95.2%, 44.5%, and 17.4% for M–Ni, non-magnetized Ni, and Cu foils, respectively (Fig. S15a–c, SI). Furthermore, the HCMASS promotes interfacial generation of additional inorganic phases including Li<sub>3</sub>N and Li<sub>2</sub>O (Fig. 3h and Fig. S15d, SI). In contrast, conventional non-magnetized Ni and Cu foils develop SEI layers predominantly composed of organic constituents with minimal LiF, Li<sub>2</sub>O, or Li<sub>3</sub>N content (Fig. S15e–g, SI). Remarkably, the HCMASS-induced SEI demonstrates exceptional stability, retaining the original MRIP-SEI composition with substantial LiF, Li<sub>2</sub>O, and Li<sub>3</sub>N components even post-cycling (Fig. S16, SI).

Three-dimensional ToF-SIMS mapping elucidates the structural hierarchy and spatial distribution of SEI components. The MRIP-SEI exhibits higher concentrations of LiF and inorganic constituents compared to the conventional SEI, particularly enriched in the middle and lower layers, which form a robust passivation architecture (Fig. 3i). Conversely, OSS-induced SEIs on non-magnetized Ni and Cu foils display complex organic–inorganic hybrids with predominant organic content (Fig. S17 and S18, SI). These organic components demonstrate limited passivation effectiveness, leaving the electrode–electrolyte interphases susceptible to persistent parasitic reactions.<sup>28</sup> Depth-resolved elemental mapping confirms LiF<sub>2</sub><sup>−</sup> dominance in the MRIP-SEI, aligning with XPS sputtering trends (Fig. 3j and k). Monochromatic gradient plots of LiF<sub>2</sub><sup>−</sup>, LiO<sup>−</sup>, LiS<sup>−</sup>, and LiCO<sub>3</sub><sup>−</sup> species reveal homogeneous inorganic distribution in the MRIP-SEI, facilitating isotropic Li<sup>+</sup> diffusion channels and superior deposition morphologies (Fig. 3l). In stark contrast, the OSS-SEI on non-magnetized Ni and Cu foils shows a highly heterogeneous distribution of these inorganic components,

promoting selective Li<sup>+</sup> diffusion/deposition that fosters dendrite growth and the formation of “dead lithium” (Fig. 3m and Fig. S19, SI). These findings establish M–Ni’s critical role in stabilizing LiF-rich SEI formation and enabling reversible electrochemical processes.

### 2.3 MRIP-SEI with both high lithium ion conductivity and strong mechanical properties

As illustrated in Fig. 4a, in the ordered inorganic–organic composite MRIP-SEI, the abundant inorganic clusters provide the SEI layer with superior mechanical properties to ensure structural integrity, while the uniform organic–inorganic spatial arrangement facilitates the construction of rapid lithium-ion diffusion pathways. The interfacial impedance of this structure is lower than that of the organic-derived SEI and completely passivated inorganic SEI (Fig. S20, SI). To systematically elucidate the superior performance of the HCMASS-induced MRIP-SEI in lithium-ion transport, interfacial kinetics, and mechanical stability, comprehensive electrochemical characterization studies were conducted. The activation energy ( $E_a$ ) for Li<sup>+</sup> migration across the SEI interface was quantitatively determined through temperature-dependent electrochemical impedance spectroscopy (EIS) analysis.<sup>14</sup> The Nyquist plots acquired at varying temperatures (30–60 °C) consistently demonstrate lower interfacial resistance ( $R_{in}$ ) for the MRIP-SEI compared to conventional Ni-SEI and Cu-SEI systems across all tested temperatures (Fig. 4b–d and Fig. S21a, b, SI). This performance enhancement originates from the unique reinforced concrete-like architecture that effectively suppresses parasitic side reactions while establishing efficient ion-conducting channels.

Arrhenius analysis of temperature-dependent  $E_a$  values reveals a reduced diffusion barrier (activation energy) for the MRIP-SEI (53.7 kJ mol<sup>−1</sup>) compared to the Ni-SEI (63.6 kJ mol<sup>−1</sup>) and Cu-SEI (76.0 kJ mol<sup>−1</sup>), providing mechanistic insight into its enhanced Li<sup>+</sup> transport efficiency (Fig. 4e and Fig. S21c, SI). Complementary Tafel analysis derived from cyclic voltammetry (CV) measurements was used to quantify the interfacial charge transfer kinetics, with exchange current density ( $j_0$ ) values calculated from polarization curves (Fig. 4f and Fig. S21d, SI). The MRIP-SEI exhibits an exceptional  $j_0$  value of 1.34 mA cm<sup>−2</sup>, outperforming the Ni-SEI (0.40 mA cm<sup>−2</sup>) and Cu-SEI (0.31 mA cm<sup>−2</sup>), confirming superior charge transfer capability and sufficient lithium flux for homogeneous deposition.

The mechanical reinforcement provided by the MRIP-SEI was systematically investigated through nanomechanical characterization. Atomic force microscopy (AFM) 3D topography reveals a more homogeneous surface morphology with reduced roughness compared to conventional SEI layers (Fig. 4g, h and Fig. S22a, SI), suggesting favorable conditions for uniform lithium nucleation. Quantitative Derjaguin–Muller–Toporov (DMT) modulus analysis derived from stress–displacement curves demonstrated remarkable mechanical enhancement, with the MRIP-SEI exhibiting an average modulus of 5.07 GPa *versus* 1.07 GPa (Ni-SEI) and 0.99 GPa (Cu-SEI) (Fig. 4i and Fig. S22b, SI). This mechanical superiority stems from the ordered inorganic-dominated architecture that functions as a

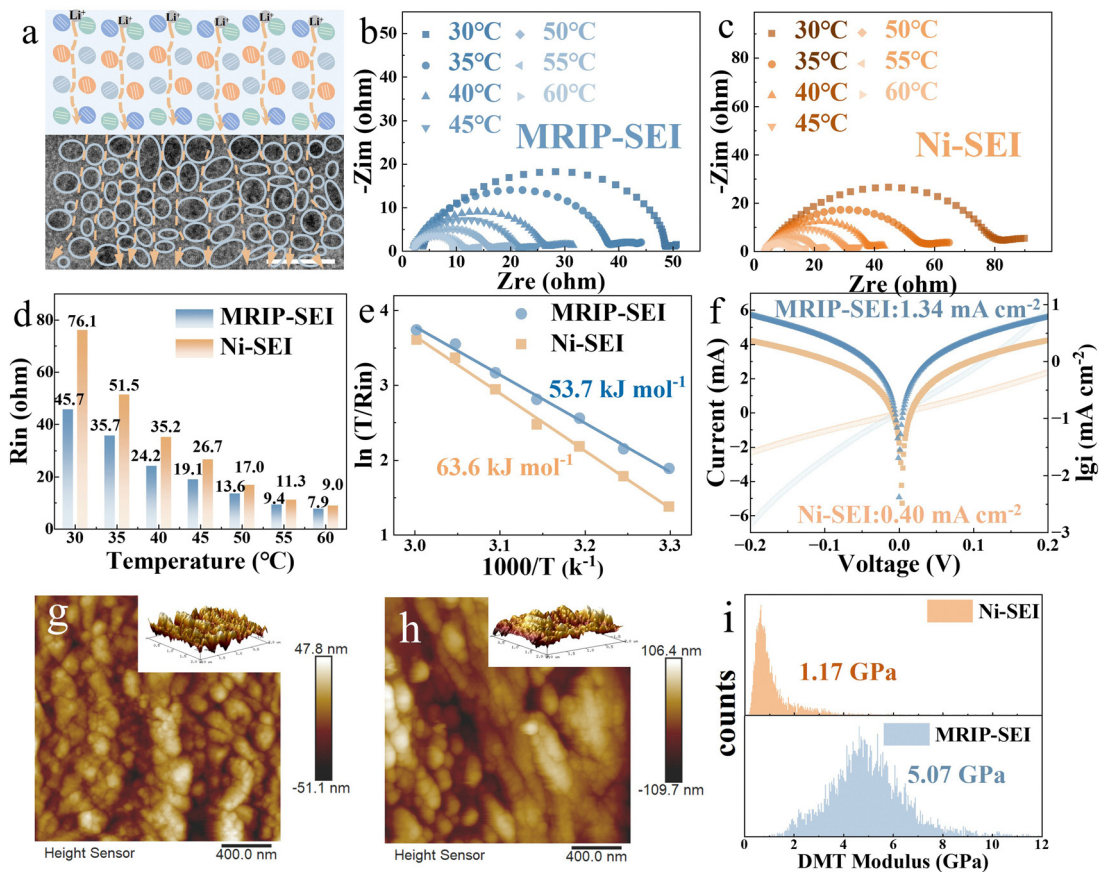


Fig. 4 Properties of SEIs. (a) Schematic diagram and cryo-TEM image of the interfacial structure and lithium ion diffusion path in the MRIP-SEI (scale bar: 10 nm). EIS after the generation of (b) the MRIP-SEI and (c) Ni-SEI at seven different temperatures (30, 35, 40, 45, 50, 55, and 60 °C). (d) Impedance comparison of the MRIP-SEI and Ni-SEI. (e) The activation energy for ion diffusion in SEI layers. (f) Tafel plots and corresponding exchange current of the MRIP-SEI and Ni-derived SEIs. (g) AFM images of the current collectors' surfaces with (g) the MRIP-SEI and (h) the Ni-SEI. (i) DMT modulus distribution of the MRIP-SEI and Ni-SEI.

strain-resistant shield during repeated lithium plating/stripping cycles.<sup>29</sup>

#### 2.4 HCMASS-induced MRIP-SEI for optimizing the behavior of lithium plating

Although previous studies have confirmed the regulatory role of external physical fields in lithium deposition behavior, a key challenge remains in developing straightforward methods for integrating external forces directly at electrode–electrolyte interphases.<sup>18</sup> In this study, we comprehensively validated the effectiveness of the MRIP-SEI through a multi-modal approach combining scanning electron microscopy (SEM), focused ion beam-SEM (FIB-SEM), *in situ* optical microscopy, and multi-physics simulations. The experimental protocol consisted of subjecting the cell to a single charge–discharge cycle to form the SEI, followed by lithium deposition at 0.1 mA cm<sup>-2</sup> to 0.15 mA cm<sup>-2</sup>. FIB-SEM characterization reveals that the HCMASS-derived MRIP-SEI induces exceptionally dense lithium deposition approaching theoretical limits (~0.73 μm) (Fig. 5a and b). In contrast, the Ni-SEI system exhibits pronounced void formation (Fig. 5c), attributed to structural and compositional heterogeneity triggering regional selective plating.

When subjected to increased current density (0.3 mA cm<sup>-2</sup>) and areal capacity (0.4 mAh cm<sup>-2</sup>), the MRIP-SEI preserves structural integrity while demonstrating void-free lithium deposition, with the deposited layer thickness reduced to one-third of control samples (Fig. 5d–f). Under extreme operational conditions (0.5 mA cm<sup>-2</sup>, 10 mAh cm<sup>-2</sup>), the MRIP-SEI effectively inhibits dendritic growth, in sharp contrast to the Ni-SEI which develops hazardous rod-like protrusions prone to dead lithium formation during cycling (Fig. 5g–i). Quantitative characterization reveals remarkably low porosity levels in the M–Ni system: 0.9% (0.1 mA cm<sup>-2</sup>) and 13.1% (0.3 mA cm<sup>-2</sup>), which correlates with the reduced deposition layer thickness and indirectly confirms the exceptional ionic conductivity and mechanical resilience of the MRIP-SEI. Comparatively, unmagnetized Ni foils exhibit higher average porosity values of 55.5% (0.1 mA cm<sup>-2</sup>) and 66.7% (0.3 mA cm<sup>-2</sup>) (Fig. 5j). Cross-sectional SEM analysis further highlights that the unoptimized solvation structure near Cu foils led to extensive void formation and dendritic crystallization (Fig. S23, SI). Post-charge/discharge-cycling SEM characterization demonstrates sustained densification of deposited layers enabled by the MRIP-SEI (Fig. S24, SI), attributable to persistent high lithium-ion flux

and maintained mechanical stability throughout charge–discharge processes.<sup>30,31</sup>

*In situ* optical microscopy further reveals distinct differences between the MRIP-SEI and the OSS-SEI. After plating at  $20 \text{ mA cm}^{-2}$ , the lithium metal with the OSS-SEI exhibits numerous loose structures (Fig. 5l), whereas the deposition morphology in the MRIP-SEI system shows no significant heterogeneous accumulation layer (Fig. 5k). These observations align with the FIB-SEM

results. COMSOL Multiphysics simulations of the phase field, concentration field, and potential field during lithium deposition reveal contrasting nucleation mechanisms (Fig. 5m, n and Fig. S25–S27, SI). In the control case, lithium demonstrates stochastic and localized nucleation, primarily forming rod-like structures accompanied by the chaotic concentration and potential distributions (Fig. 5m). While this represents an improvement over the single-site deposition morphology, such



**Fig. 5** Deposition behaviors on various current collectors. (a) Charge/discharge profiles and corresponding FIB-SEM images with (b) the MRIP-SEI and (c) the Ni-SEI at  $0.1 \text{ mA cm}^{-2}$ . (d) Charge/discharge profiles and corresponding FIB-SEM images with (e) the MRIP-SEI and (f) the Ni-SEI at  $0.3 \text{ mA cm}^{-2}$ . (g) Charge/discharge profiles and corresponding SEM images with (h) the MRIP-SEI and (i) the Ni-SEI at  $0.5 \text{ mA cm}^{-2}$ . (j) Comparison of porosity of lithium deposition layers induced by different current collectors. Morphological evolution of electrodeposited Li characterized by real-time optical microscopy with (k) the MRIP-SEI and (l) the Ni-SEI. Phase field simulation results of lithium deposition induced by (m) heterogeneous nucleation (Ni-SEI) and (n) uniform nucleation (MRIP-SEI).

heterogeneous deposition behavior remains challenging for achieving high efficiency and long-term cycling stability in anode-free cells. In contrast, the multi-site homogeneous nucleation process with the MRIP-SEI (M-Ni) yields a dense lithium deposition morphology with minimal branching (Fig. 5n). This plating behavior closely resembles ideal uniform deposition, accompanied by the stable lithium-ion concentration and potential distributions, highlighting the superior interfacial stability enabled by the MRIP-SEI.

## 2.5 MRIP-SEI to optimize interfacial mass transfer for high-performance anode-free lithium metal batteries

The MRIP-SEI interfacial layer demonstrates remarkably enhanced electrochemical properties across multiple battery configurations. Lithium symmetric cells incorporating the MRIP-SEI exhibit cycling stability exceeding 5000 hours at  $2 \text{ mA cm}^{-2}$ , outperforming conventional Ni-SEI systems by 12-fold and 20-fold, respectively (Fig. 6a and Fig. S28, SI). Notably, symmetric cells enabled by the MRIP-SEI maintain a stable low overpotential of  $\pm 70 \text{ mV}$  throughout cycling (Fig. 6b), indicating homogeneous lithium deposition and stripping. In contrast, Ni-SEI and Cu-SEI counterparts exhibit progressively increasing and unstable overpotentials. From the comparison of FIB-SEM images, it can be seen that after cycling, the lithium plating layer induced by the MRIP-SEI is still very dense and there are no large voids. In contrast, the lithium plating process under the OSS-SEI is very uneven, with a large number of voids, which easily produces

dead lithium and causes continuous loss of active lithium (Fig. 6c). To assess lithium cycling reversibility, Li||Cu half-cells were fabricated for CE measurements. The MRIP-SEI-based half-cells achieve over 1400 reversible cycles at  $0.5 \text{ mA cm}^{-2}$ , demonstrating 15-fold greater cycle longevity compared to Ni-SEI and Cu-SEI systems (Fig. 6d, e and Fig. S29, SI). Particularly noteworthy is their sustained operation beyond 500 cycles at  $1 \text{ mA cm}^{-2}$  (Fig. S30, SI), coupled with an average CE of 99.8% at  $2 \text{ mA cm}^{-2}$  (Fig. 6f), establishing critical technical foundations for anode-free full-cell configurations. Compared with some previously reported literature, the Li||Cu half-cell exhibits longer cycling stability and a higher average CE (Table S2, SI).

This performance superiority extends to anode-less Cu@Li||LFP full-cell configurations. The full cell dominated by the MRIP-SEI layer exhibits excellent stability, maintaining more than 80% capacity retention after 1000 cycles at a 0.5C rate (N/P = 0.8), while the cell with the Ni-SEI layer shows rapid capacity decay starting from the 370th cycle (Fig. 6g and Fig. S31, SI). Alarming, Cu-SEI-based lithium metal batteries suffer from catastrophic capacity collapse, resulting in below 60% retention after merely 45 cycles (Fig. S32, SI). Compared with the full lithium metal cells reported in recent literature, the ultra-stable cycling performance demonstrated in this work shows remarkable competitiveness in terms of long-term operational durability (Fig. S33, and detailed data can be found in Table S3, SI). Under anode-less conditions (N/P = 0.3), MRIP-SEI-enabled cells preserve >85% capacity retention with a

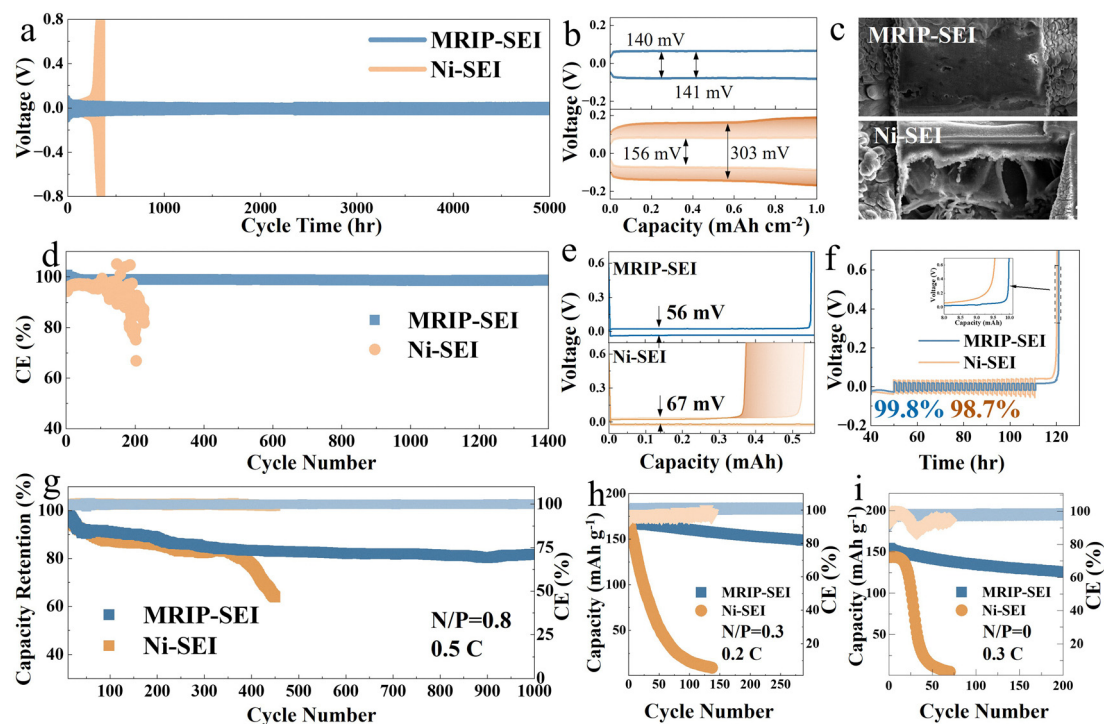


Fig. 6 MRIP-SEI to optimize interfacial mass transfer for high-performance anode-free and anode-less lithium batteries. (a) Comparison of cycling performance and (b) charging/discharging curves of Li||Li symmetrical cells at  $2 \text{ mA cm}^{-2}$ . (c) FIB-SEM images with the MRIP-SEI and Ni-SEI after cycling. (d) Comparison of cycle performance of Li||Cu cells and (e) corresponding charging/discharging curves at  $0.5 \text{ mA cm}^{-2}$ . (f) Aurbach average CE of Li||Cu cells at  $2 \text{ mA cm}^{-2}$ . (g) Cycling performance of Cu@Li||LFP full cells at 0.5C (N/P ~ 0.8). (h) Cycling performance of anode-less Cu@Li||LFP full cells at 0.2C (N/P ~ 0.3). (i) Cycling performance of anode-free Cu||LFP full cells at 0.3C (N/P = 0).

specific discharge capacity of  $150 \text{ mAh g}^{-1}$  through 300 cycles (Fig. 6h). In contrast, Ni-SEI systems display precipitous capacity degradation trajectories, collapsing to  $<20\%$  retention within 100 cycles. Notably, under anode-free conditions ( $N/P = 0$ ), the capacity retention of the Cu||LFP cell with the MRIP-SEI is higher than 80% after 200 cycles, while the capacity of the Cu||LFP cell with the Ni-SEI and Cu-SEI decays to nearly 0 mAh after 70 and 60 cycles, respectively (Fig. 6i, and Fig. S34, S35, SI).

## 2.6 Enhancing the CEI by HCMASS for stable high-voltage anode-free Cu||NCM811 batteries

Although ether-based electrolytes exhibit excellent compatibility with lithium metal anodes, their implementation in high-voltage NCM811 cathode systems is hindered by persistent parasitic reactions that accelerate capacity degradation. Our investigation reveals that HCMASS extends its interfacial optimization capabilities to the CEI through ILF and IEF driving during the discharge process, forming a MRIP-CEI analogous to the MRIP-SEI (Fig. 1c). To verify whether the HCMASS has accumulated on the cathode side, *in situ* Raman spectroscopy was used to detect the real-time changes in the electrolyte solvation structure near the cathode surface. As shown in Fig. S36, the signals of the electrolyte near the cathode exhibit the strongest intensity at  $745 \text{ cm}^{-1}$  Raman shift, indicating a strong interaction between anions and cations, which manifests as the presence of contact ion pairs (CIPs) on the cathode side. Further detailed analysis of these peaks reveals that their intensity increases along with the charge/discharge cycling, suggesting a significant rise in the quantity of CIPs. This trend may be attributed to the migration of lithium ions from the anode to the cathode during discharge, leading to the accumulation of the HCMASS on the cathode side. Comparison of this Raman spectrum with that of an OSS shows a clear redshift from  $\sim 742 \text{ cm}^{-1}$  to  $\sim 745 \text{ cm}^{-1}$ , indicating that most of the anions near the cathode participate in the solvation structure of  $\text{Li}^+$ , forming a HCMASS. Furthermore, *in situ* Raman spectroscopy reveals a significant intensity change at a Raman shift of  $\sim 941 \text{ cm}^{-1}$  (Fig. S36d, SI). This relatively strong solvent peak observed during charging gradually weakened during discharging, indicating that HCMASS has a shielding effect on free solvents at both the anode and the cathode. To verify the universality of this strategy, HCMASS aggregation at the electrode-electrolyte interface is still observed in localized high concentration ether-based electrolytes (LHCEE) (Fig. S37, SI). Therefore, the ILF generated by M-Ni not only affects the anode but also modulates the cathode interface environment by forming a HCMASS in the electrolyte, demonstrating a certain degree of versatility. The accumulation of HCMASS on the cathode promotes the formation of anion-derived inorganic-rich CEIs.

This dual-functional interphase not only suppresses electrolyte decomposition but also stabilizes the cathode structure during lithium intercalation/deintercalation. Cryo-TEM characterization demonstrates that the MRIP-CEI induced by HCMASS maintains a uniform thickness of 10 nm (Fig. 7a), in stark contrast to the irregular OSS-derived CEI (5–39 nm thickness variations) (Fig. 7b), which promotes localized

lithium-ion flux accumulation in thinner regions, ultimately inducing particle cracking. High-resolution cryo-TEM imaging and selected area electron diffraction (SAED) confirm the abundant presence of inorganic components such as LiF within the MRIP-CEI (Fig. 7c and d), while XPS analysis quantitatively verifies its LiF-rich composition, providing essential mechanical reinforcement (Fig. 7e and Fig. S38, SI). AFM characterization further confirms the interfacial strengthening effect of the MRIP-CEI, and the DMT modulus of NCM811 particles under the protection of MRIP-CEI is 28.8 GPa, while that of NCM811 particles with the OSS-derived CEI is only 5.6 GPa after cycling tests (Fig. 7f and g). Cryo-TEM and XPS analyses of the NCM811 material after cycling further reveal that the MRIP-CEI layer exhibits exceptional stability (Fig. S39 and S40, SI), retaining its original thickness and uniform structure (10 nm), while remaining abundant in LiF.

The LSV curves confirm that the CEI generated under the influence of M-Ni effectively slows down the oxidative decomposition of the electrolyte (Fig. S41, SI). The stable operating voltage window increases from approximately 4.0 V to around 4.5 V (vs.  $\text{Li/Li}^+$ ), with the decomposition current remaining below  $2.2 \mu\text{A cm}^{-2}$  ( $0.5 \text{ mV s}^{-1}$ ). *In situ* EIS and distribution of relaxation time (DRT) techniques were performed to decouple specific electrochemical processes on a time scale. Tracking the relaxation time identifications helps reveal the electrode-electrolyte interphase chemistry during cycling. As shown in Fig. 7h,  $\tau_1$  at  $10^{-5} \text{ s}$  can be assigned to the contact resistance corresponding to the electrolyte resistance. In addition, the peaks  $\tau_2$  (at  $10^{-4}$  to  $10^{-3} \text{ s}$ ) and  $\tau_3$  (at  $10^{-3}$  to  $10^{-2} \text{ s}$ ) indicate that ions transport through the CEI/SEI layer. The DRT spectra show a peak at  $10^{-2} \text{ s}$ , corresponding to the charge transfer resistance ( $\tau_4$ ), and the peaks ( $\tau_5, \tau_6$ ) at  $10^{-1}$  to 10 s indicate mass transfer. It is worth noting that in the control case (without M-Ni), obvious peaks are observed at  $\tau_2$  and  $\tau_3$  due to the large impedance of the CEI and SEI. This high charge/discharge resistance between NCM811 and the electrolyte severely hinders the ion diffusion. In contrast, the NCM811 cell with M-Ni maintains a relatively low interfacial resistance, indicating that the MRIP-CEI has fast lithium ion diffusion channels. This optimized ion transport pathway enables highly reversible lithium ion migration, and FIB-SEM confirms the structural integrity of the MRIP-CEI-protected cathode particles, while a large number of voids are formed in the unmodified cathode particles (Fig. 7i and j).

The MRIP-CEI combines rapid ion diffusion capabilities with strong mechanical stability, enabling the high-nickel NCM811 cathode material to operate stably under high-voltage conditions in an ether electrolyte, with BTFE as the baseline additive (Fig. S42, SI). The NCM811 pouch cell ( $\sim 760 \text{ mAh}$ ) with the MRIP-CEI exhibits minimal capacity decay over 1000 cycles, with a fading rate of only 0.007% per cycle (Fig. S43, SI). Further practical validation in a full-cell configuration demonstrated outstanding performance. As shown in Fig. 7k and Fig. S44, S45, the Cu||NCM811 full cell with the MRIP-CEI achieves 91.6% capacity retention over 100 cycles, instead of the 25.2% by the Cu@Ni||NCM811 cell (after 50 cycles) and 12.4% by the



Fig. 7 MRIP-CEI to enhance cathode stability for anode-free Cu||NCM811 batteries. Cryo-TEM images of the CEI morphology with (a) the MRIP-CEI and (b) the OSS-CEI. (c) and (d) High-resolution cryo-TEM images of the CEI morphology of the MRIP-CEI (scale bar: 1 nm;  $5 \text{ nm}^{-1}$ ). (e) XPS spectra of F 1s of the MRIP-CEI and the OSS-CEI. AFM images and DMT modulus distribution of (f) the MRIP-CEI and (g) the OSS-CEI. (h) Contour plots of the corresponding DRT results for the NCM811 cell with the MRIP-CEI and the OSS-CEI during charging/discharging processes. FIB-SEM images of NCM811 particles after cycling tests with (i) the OSS-CEI and (j) the MRIP-CEI. (k) Cycling performance of Cu||NCM811 full cells. (l) Cycling performance of anode-free Cu||NCM811 cells at 0.5C with a cut-off voltage of 4.5 V. (m) Charging/discharging curves of the anode-free Cu||NCM811 pouch cell.

Cu||NCM811 cell (after 15 cycles) with the OSS-CEI. In addition, when cycled up to 4.5 V, the Cu||NCM811 cell with the MRIP-CEI delivers a specific discharge capacity exceeding  $190 \text{ mAh g}^{-1}$ , while still maintaining over 75% capacity retention after 100 cycles (Fig. 7l). Notably, the 2.45 Ah-level anode-free Cu||NCM811 pouch cell design achieves stable cycling for over 50 cycles and delivers an energy density of  $453.5 \text{ Wh kg}^{-1}$  (Fig. 7m).

### 3. Conclusions

In summary, we propose a straightforward and effective strategy for developing anode-free lithium metal batteries through surface modification by helical counter-directional migration-induced anion-derived solvation sheaths. During the formation process, the ILF effect optimizes the migration pathways and association/dissociation behavior of electrolyte ions, directing

anions to concentrate in the solvation structure of counter-migrating lithium ions. This innovative approach enables the formation of a robust SEI layer characterized by an ordered inorganic particle skeleton filled with organic components, which combines high mechanical strength and rapid ion permeability. This synergistic interaction facilitates favorable interfacial reactions, ultimately establishing a durable electrode–electrolyte interphase. The modified Cu electrode demonstrates an outstanding CE of 99.9%, and the lithium symmetric battery operated stably for more than 5000 hours. The anode-less (N/P = 0.8) lithium-metal full cells maintain over 80% capacity retention after 1000 stable cycles, and the capacity retention of the anode-free Cu||LFP cell with the MRIP-SEI is higher than 80% after 200 cycles. Notably, the HCMASS simultaneously optimizes the CEI layer through ILF and IEF driving, enabling stable operation of NCM811 cathodes in ether-based electrolytes. Anode-free Cu||NCM811 cells cycled in ether-based electrolytes at 4.5 V exhibit a capacity retention exceeding 75% after 100 cycles and realize a 453.5 Wh kg<sup>-1</sup> anode-free lithium metal pouch cell configuration. Our work establishes a practical pathway for developing high-energy-density anode-free lithium metal batteries through this simple yet effective interfacial engineering approach.

## 4. Experimental

### 4.1 Materials

The lithium metal anodes were obtained from China Energy Lithium Co., Ltd. Lithium iron phosphate (LiFePO<sub>4</sub>, LFP), lithium nickel cobalt manganese oxide (LiNi<sub>0.8</sub>Co<sub>0.1</sub>Mn<sub>0.1</sub>O<sub>2</sub>, NCM811) cathodes, and the ether-based electrolyte of 1.2 M LiTFSI-1,3-dioxolane (DOL)/1,2-dimethoxyethane (DME) (vol/vol = 1)–1%LiNO<sub>3</sub> and 1.2 M LiFSI-DOL/DME/ethylene glycol dibutyl ether (EGDBE)/bis(2,2,2-trifluoroethyl)ether (BTFE)–1% LiNO<sub>3</sub> were procured from Kelude Corporation, with all materials incorporated into the electrolytes within an argon-filled glovebox maintaining strict atmospheric control (H<sub>2</sub>O < 0.1 ppm and O<sub>2</sub> < 0.1 ppm). Cu foils with different nickel layer thicknesses were obtained by electroplating. Neodymium iron boron was used as a magnetic field generator.

### 4.2 Electrochemical measurement

**4.2.1 Electrochemical measurements of Li||Cu cells.** All electrochemical evaluations were performed using two-electrode CR2032 coin cells. Li||Cu cells were assembled to assess the cycling performance, conduct electrochemical analysis, and characterize morphological evolution. CE was evaluated *via* two independent methods: the conventional CE test and the Aurbach method.<sup>32</sup> Prior to cell assembly, copper current collectors were modified by attaching metal particles of different morphologies. To prevent direct reduction of the silver initiator on the lithium metal surface, a passivation layer was pre-coated on the counter electrode. For comprehensive electrochemical characterization (EIS and LSV), Cu@Li electrodes were prepared by pre-depositing 0.5 or 1.0 mAh cm<sup>-2</sup> of lithium onto copper substrates at a current density of 0.1 mA cm<sup>-2</sup>.

Symmetric cell cycling was carried out at a current density of 1.0 or 2.0 mA cm<sup>-2</sup>. Electrochemical measurements (EIS and CV) were conducted on a CHI660E/760E electrochemical workstation (Shanghai Chenhua). EIS spectra were collected over a frequency range of 0.1 Hz to 10<sup>5</sup> Hz at temperatures between 30 and 60 °C, and the resulting impedance data were analyzed using ZView software to extract interfacial diffusion parameters. CV measurements were performed at a scan rate of 10 mV s<sup>-1</sup> within a potential window of –0.2 to 0.2 V.

The interfacial diffusion activation energy based on the temperature-dependent EIS results was calculated using the Arrhenius equation:

$$\frac{T}{R_{in}} = Ae^{(-E_a/RT)}$$

where  $R_{in}$  is the ion transfer resistance of the interface,  $T$  is the temperature,  $A$  is the pre-exponential constant,  $E_a$  is the activation energy of Li<sup>+</sup> diffusion when transporting through the interface, and  $R$  is the standard gas constant. The Tafel plots of all samples were probed and obtained from the CV profiles. The exchange current ( $j_0$ ) was calculated from the corresponding Tafel plots to reflect charge-transfer kinetics in various SEIs. The process began by extracting the overpotential ( $\eta$ ) and current density ( $j$ ) data. The analysis relies on the Butler–Volmer equation. For the primary Tafel analysis, the data at higher overpotentials (where the system displays mixed kinetic control) were plotted as  $\eta$  versus  $\log|j|$ . The linear portions of these curves were fitted to the Tafel equation,

$$\log|j| = \log|j_0| \pm \frac{(1-\alpha)nF}{2.303RT}\eta$$

where  $j_0$  denotes the exchange current density,  $\alpha$  represents the charge transfer coefficient,  $F$  is the Faraday constant,  $R$  indicates the gas constant, and  $T$  is the absolute temperature.

The porosity ( $P$ ) of the Li deposit was then determined by calculating the volume fraction occupied by voids, derived from the ratio of the theoretical ( $d_t$ ) to actual thickness ( $d_a$ ):

$$P (\%) = \left(1 - \frac{d_t}{d_a}\right) \times 100\%$$

where  $d_a$  was directly obtained from statistical analysis of the FIB-SEM images,  $d_t$  is obtained from the theoretical density and capacity of the lithium metal.

**4.2.2 Full cell assembly and electrochemical measurements.** Cu||LFP coin cells were employed to evaluate rate capability and cycling performance at various rates. Pouch cells were used to study anode-free full cells. NCM811 (96.7% active materials, ~22 mg cm<sup>-2</sup>) was used as the cathode material, and bare Cu (8 μm) was used as the anode current collector. The pouch cells were filled with 2.0 g of liquid electrolyte before being vacuum sealed. The pouch cells were cycled at 0.1C charge and discharge between 2.8 V and 4.3 V after the initial activation, at a 0.5C charge–discharge rate. The total pouch cell capacity was about 2.5 Ah under these conditions. In addition, a 0.8 Ah pouch cell with a graphite anode and a NCM811 cathode was assembled.

The DRT analysis was employed to deconvolve the overlapping electrochemical processes in the measured *in situ* EIS data of the Li||NCM811 cell. Regarding the specific data acquisition process, the DRT was indeed calculated using a well-established and publicly available MATLAB toolbox developed by the Ciucci research group.<sup>33</sup> The process involved importing the raw EIS data directly into this specialized software. The resulting DRT plot, which presents the polarization resistance as a distribution of relaxation times, was then used to identify the characteristic frequencies of the various electrochemical processes based on their well-documented time constants in the literature.<sup>34</sup>

**4.2.3 Characterization.** Cryo-TEM characterization was performed on a Thermo Scientific Glacios cryo-TEM microscope operated at 200 keV to analyze the composition and structure of the SEI. ToF-SIMS (IonTof M6 Hybrid) was also used to investigate SEI components. AFM (Dimension ICON) was used to analyze the DMT modulus. *In situ* Raman spectroscopy was performed under 785 nm laser excitation (Invia). The morphology of the deposited Li was determined using an extremely high-resolution scanning electron microscope (SEM, JSM 7800F, JEOL). The operation voltage of the SEM was 10.0 kV or 15.0 kV. The morphology of lithium deposition/stripping and the integrity of the SEI were explored by SEM after long-term cycles. The cross-sectional morphology was determined using a focused ion beam-scanning electron microscope (FEI Helios G4 UX). Rough cross-sectional milling (30 kV, 1000 pA) was performed on the anode by the FIB (Ga beam). XPS measurements were performed with a Surface Analysis Kratos Axis Supra+ to investigate the chemical compositions of the plating electrodes. The samples were transferred into the XPS machine under vacuum using an air-tight sample holder.

**4.2.4 COMSOL simulation.** A simplified two-dimensional model was established to investigate lithium deposition morphologies on substrates with varying densities of active nucleation sites. The model couples the Butler-Volmer equation for electrochemical kinetics at the electrode surface with Fick's law for ion concentration diffusion and the Nernst-Einstein relationship for ion migration. The simulation domain, set to  $50 \times 25 \mu\text{m}^2$ , was discretized using a fine triangular mesh. A comparative analysis was performed across substrates with differing numbers of active sites to elucidate their influence.

For the exploration of helical migration, in terms of the computational domain and electrodes, the overall model was a cylinder. The top is a flat circular lithium metal electrode, serving as the emission source of lithium ions. The bottom was a copper electrode, designed with a central protrusion. This protrusion was used to alter the electric field distribution in the bottom space, thereby simulating the effect of microscopically rough electrode surfaces on ion motion. The space between the two electrodes was filled with an electrolyte medium. The main simulation workflow includes the following: initialization: set the initial position and initial velocity (typically zero or a very small random value) of the particles on the surface of the top lithium electrode; time stepping: for each particle, apply the RK4 method to iteratively update its position and velocity; termination check: after each iteration step, check the

following termination conditions; particle reaches the collector: when the distance between the particle and the surface of the bottom copper electrode is less than a set threshold, the particle is considered successfully collected, and its trajectory and time of flight are recorded.

**4.2.5 MD simulation.** MD simulations were carried out using the Forcite module within the Materials Studio software package (2020 release) to investigate the role of M-Ni in modulating the solvation sheath structure. The simulation system was constructed to closely mimic experimental conditions. Initially, molecules were randomly packed into a cubic box with dimensions of 60 Å along the *x*, *y*, and *z* axes. After pre-equilibration in the isothermal-isobaric (NPT) ensemble, the box size stabilized at 56.3 Å. All MD simulations employed the COMPASS II (Condensed-phase Optimized Molecular Potentials for Atomistic Simulation Studies II) forcefield, which is suitable for systems comprising both organic and inorganic components and accurately reproduces the structure and properties of condensed phases, making it well-suited for modeling the electrolyte system under study. Electrostatic interactions were treated using the particle-particle particle-mesh (PPPM) method.

## Author contributions

Y. C. and M. S. conceived the concept and the project. Y. C. conducted all experiments, measurements, and calculations. Y. L., X. Q., Y. Q., Y. T. K., S. Z., X. L., and S. L. were involved in the discussions. All authors participated in the analysis of the results and reviewed the manuscript.

## Conflicts of interest

The authors declare no competing interest.

## Data availability

The data that support the findings of this study are available from the corresponding author on reasonable request.

Supplementary information (SI): supplementary Fig. S1–S45 and Tables S1–S3. See DOI: <https://doi.org/10.1039/d5ee06208j>.

## Acknowledgements

This work is supported by the National Natural Science Foundation of China (project no. 22408064), the Hong Kong Research Grant Council (R6011-23, JLFS/P-602/24), the Guangzhou Science and Technology Bureau (2024A03J0609), the Guangzhou Nansha Science & Technology Bureau (2024ZD009), Otto Poon Center for Climate Resilience and Sustainability, and the LKS Fellowship from Biological Cryo-EM Center, HKUST.

## References

- I. R. Choi, Y. Chen, A. Shah, J. Florian, C. Serrao, J. Holoubek, H. Lyu, E. Zhang, J. H. Lee, Y. Lin, S. C. Kim,

- H. Park, P. Zhang, J. Lee, J. Qin, Y. Cui and Z. Bao, *Nat. Energy*, 2025, **10**, 365–379.
- 2 Y. Lu, Q. Cao, W. Zhang, T. Zeng, Y. Ou, S. Yan, H. Liu, X. Song, H. Zhou, W. Hou, P. Zhou, N. Hu, Q. Feng, Y. Li and K. Liu, *Nat. Energy*, 2025, **10**, 191–204.
- 3 C. Jin, Y. Huang, L. Li, G. Wei, H. Li, Q. Shang, Z. Ju, G. Lu, J. Zheng, O. Sheng and X. Tao, *Nat. Commun.*, 2023, **14**, 8269.
- 4 Y. Xia, P. Zhou, X. Kong, J. Tian, W. Zhang, S. Yan, W.-H. Hou, H.-Y. Zhou, H. Dong, X. Chen, P. Wang, Z. Xu, L. Wan, B. Wang and K. Liu, *Nat. Energy*, 2023, **8**, 934–945.
- 5 M. Mao, X. Ji, Q. Wang, Z. Lin, M. Li, T. Liu, C. Wang, Y.-S. Hu, H. Li, X. Huang, L. Chen and L. Suo, *Nat. Commun.*, 2023, **14**, 1082.
- 6 J. Shi, T. Koketsu, Z. Zhu, M. Yang, L. Sui, J. Liu, M. Tang, Z. Deng, M. Liao, J. Xiang, Y. Shen, L. Qie, Y. Huang, P. Strasser and J. Ma, *Nat. Mater.*, 2024, **23**, 1686–1694.
- 7 T. Fuchs, T. Ortman, J. Becker, C. G. Haslam, M. Ziegler, V. K. Singh, M. Rohnke, B. Mogwitz, K. Peppler, L. F. Nazar, J. Sakamoto and J. Janek, *Nat. Mater.*, 2024, **23**, 1678–1685.
- 8 Q. Xu, T. Li, Z. Ju, G. Chen, D. Ye, G. I. N. Waterhouse, Y. Lu, X. Lai, G. Zhou, L. Guo, K. Yan, X. Tao, H. Li and Y. Qiu, *Nature*, 2025, **637**, 339–346.
- 9 K. Huang, S. Bi, B. Kurt, C. Xu, L. Wu, Z. Li, G. Feng and X. Zhang, *Angew. Chem., Int. Ed.*, 2021, **133**, 19381–19389.
- 10 S. Jurng, Z. L. Brown, J. Kim and B. L. Lucht, *Energy Environ. Sci.*, 2018, **11**, 2600–2608.
- 11 P. Liu, S. Shen, Z. Qiu, T. Yang, Y. Liu, H. Su, Y. Zhang, J. Li, F. Cao and Y. Zhong, *Adv. Mater.*, 2024, **36**, 2312812.
- 12 S. Kim, J. H. Jeon, K. Park, S. H. Kweon, J.-H. Hyun, C. Song, D. Lee, G. Song, S.-H. Yu, T. K. Lee, S. K. Kwak, K. T. Lee, S. Y. Hong and N.-S. Choi, *Adv. Mater.*, 2024, **36**, 2401615.
- 13 J. Liu, W. Hao, M. Fang, X. Chen, Y. Dong, Y. Chen, Z. Wang, X. Yue and Z. Liang, *Nat. Commun.*, 2024, **15**, 9356.
- 14 W. Liu, T. Xie, X. Wang, W. Deng, L. Huang, R. Khan, Y. Wang, H. Hou, D. Wang and Y. Wu, *Adv. Funct. Mater.*, 2024, **34**, 2410843.
- 15 H. Song, J. Lee, M. Sagong, J. Jeon, Y. Han, J. Kim, H.-G. Jung, J.-S. Yu, J. Lee and I.-D. Kim, *Adv. Mater.*, 2024, **36**, 2407381.
- 16 F. Zhao, P. Zhai, Y. Wei, Z. Yang, Q. Chen, J. Zuo, X. Gu and Y. Gong, *Adv. Sci.*, 2022, **9**, 2103930.
- 17 Y. Chen, X. Dou, K. Wang and Y. Han, *Adv. Energy Mater.*, 2019, **9**, 1900019.
- 18 Y. Chen, H. Huang, L. Liu, Y. Chen and Y. Han, *Adv. Energy Mater.*, 2021, **11**, 2101774.
- 19 Y. Chen, Y. Chen, R. Wang, X. Lv and Y. Han, *Chem. Eng. J.*, 2022, **446**, 137435.
- 20 Y. Chen, H. Liu, L. Liu, J. Li and Y. Han, *Batteries Supercaps*, 2024, **7**, e202300389.
- 21 J. Holoubek, H. Liu, Z. Wu, Y. Yin, X. Xing, G. Cai, S. Yu, H. Zhou, T. A. Pascal, Z. Chen and P. Liu, *Nat. Energy*, 2021, **6**, 303–313.
- 22 S. Zhu and J. Chen, *Energy Storage Mater.*, 2022, **44**, 48–56.
- 23 Q. Li, G. Liu, Y. Chen, J. Wang, P. Kumar, H. Xie, W. Wahyudi, H. Yu, Z. Wang, Z. Ma and J. Ming, *Adv. Funct. Mater.*, 2025, **35**, 2420327.
- 24 X. Wang, M. Chen, S. Li, C. Zhao, W. Zhang, Z. Shen, Y. He, G. Feng and Y. Lu, *ACS Cent. Sci.*, 2021, **7**, 2029–2038.
- 25 D. Huang, C. Zeng, M. Liu, X. Chen, Y. Li, J. Zou, Q. Pan, F. Zheng, H. Wang and Q. Li, *Small*, 2025, 2412259.
- 26 P. Zhai, Q. He, H. Jiang, B. Gao, B. Zhang, Q. Chen, Z. Yang, T. Wang and Y. Gong, *Adv. Energy Mater.*, 2024, **14**, 2302730.
- 27 H. Zhuang, H. Xiao, T. Zhang, F. Zhang, P. Han, M. Xu, W. Dai, J. Jiao, L. Jiang and Q. Gao, *Angew. Chem., Int. Ed.*, 2024, **63**, e202407315.
- 28 S. Liu, X. Ji, N. Piao, J. Chen, N. Eidson, J. Xu, P. Wang, L. Chen, J. Zhang, T. Deng, S. Hou, T. Jin, H. Wan, J. Li, J. Tu and C. Wang, *Angew. Chem., Int. Ed.*, 2021, **60**, 3661–3671.
- 29 H. Liu, F. Zhen, X. Yin, Y. Wu, K. Yu, X. Kong, S. Ding and W. Yu, *Angew. Chem., Int. Ed.*, 2025, **64**, e202414599.
- 30 J. Xiao, *Science*, 2019, **366**, 426–427.
- 31 A. Jana, S. I. Woo, K. S. N. Vikrant and R. E. García, *Energy Environ. Sci.*, 2019, **12**, 3595–3607.
- 32 T. Ma, Y. Ni, Q. Wang, W. Zhang, S. Jin, S. Zheng, X. Yang, Y. Hou, Z. Tao and J. Chen, *Angew. Chem., Int. Ed.*, 2022, **134**, e202207927.
- 33 T. H. Wan, M. Saccoccio, C. Chen and F. Ciucci, *Electrochim. Acta*, 2015, **184**, 483–499.
- 34 Y. Lu, C.-Z. Zhao, J.-Q. Huang and Q. Zhang, *Joule*, 2022, **6**, 1172–1198.